


ORIGINAL RESEARCH OPEN ACCESS

Thermal Effect and Hydrodynamic Perturbation in a Coplanar Nanosecond Pulse Periodic Surface Dielectric Barrier Discharge

 Bin Zhang¹  | Xiaobing Zhang² | Bayu Dharmaputra³ | Nicolas Noiray³ | Sergey A. Shcherbanev³ | Yifei Zhu⁴

¹College of Automation Engineering, Nanjing University of Aeronautics and Astronautics, Nanjing, China | ²School of Energy and Power Engineering, Nanjing University of Science and Technology, Nanjing, China | ³CAPS Laboratory, Department of Mechanical and Process Engineering, ETH Zurich, Zurich, Switzerland | ⁴School of Electrical Engineering, Xi'an Jiaotong University, Xi'an, China

Correspondence: Yifei Zhu (yifei.zhu.plasma@gmail.com)

Received: 23 July 2024 | **Revised:** 23 November 2024 | **Accepted:** 3 December 2024

Associate Editor: Yangyang Fu

Funding: This study was supported by National Natural Science Foundation of China (Nos. 52277168, 12505232) and European Research Council under the ERC Consolidator Grant TORCH (2019-2024), (Grant 820091).

ABSTRACT

The thermal effect and hydrodynamic perturbation within a high-frequency pulse-periodic nanosecond coplanar surface dielectric barrier discharge (ncSDBD), are studied experimentally and numerically. The discharge is initiated in a coplanar open electrodes arrangement with 10 mm inter-electrode gap for pulse repetition frequencies (PRF) between 10 and 100 kHz. The discharge morphology, heat release, ozone distribution and refractive index perturbation with different repetition frequency are measured by intensified charge-coupled device (ICCD) imaging, spatially resolved emission spectroscopy, optical absorption methods and the background-oriented schlieren technique, respectively. With the increase of frequency and number of pulses, the discharge morphology changes from quasi-uniform structure at 10 kHz to filamentary mode, and a higher gas temperature is observed near the grounded electrode. In turn, the gas heating largely determines the dynamics of ozone. The discharge characteristics and hydrodynamic perturbation are modelled and analysed numerically. The existence of the exposed grounded electrode facilitates the connection between the positive and negative discharges. During the afterglow phase, a large amount of positive charge accumulates near the two exposed electrodes due to charge separation, resulting in a strong body force, which triggers the blowing up of the flow.

1 | Introduction

Over the past 2 decades, surface dielectric barrier discharges (SDBDs) have garnered significant interest. SDBDs are constructed with the high-voltage (HV) electrode situated on the dielectric layer, whereas the grounded electrode is buried beneath it. Generally, typical SDBD plasma actuators are driven by high voltage waveforms, and surface discharges are produced from HV electrode and spread across the dielectric surface. It consists of numerous microdischarges in the form of streamers,

diffuse or filamentary discharges, depending on the voltage polarity and gas pressure [1–3].

In general, sinusoidal AC voltages are employed. The physical mechanism of flow control results from the electrodynamic force induced from the interaction between surface discharges and near-wall flow [4, 5]. More recently, nanosecond pulses are used to replace the AC waveform, which has been demonstrated to provide effective control of flow separation over a wide range of Reynolds numbers [6, 7]. Different from the AC voltages, the

This is an open access article under the terms of the [Creative Commons Attribution-NonCommercial](https://creativecommons.org/licenses/by-nc/4.0/) License, which permits use, distribution and reproduction in any medium, provided the original work is properly cited and is not used for commercial purposes.

© 2025 The Author(s). *High Voltage* published by John Wiley & Sons Ltd on behalf of The Institution of Engineering and Technology and China Electric Power Research Institute.

feature of nanosecond surface dielectric barrier discharge (nSDBD) is the fast gas heating (FGH) generated from the relaxation of electronically excited states [8, 9], which results in pressure waves propagating above the dielectric surface [10, 11]. Experimental observations reveal a hemispherical shock wave due to FGH near the HV electrode and a planar shock wave resulting from streamer propagation [7, 12, 13].

In order to enhance the interaction area and electrical energy in practical application of flow control, a three-electrode configuration is developed. This configuration consists of two electrodes embedded on opposite sides of a dielectric, similar to a traditional SDBD device, plus an additional exposed electrode. Unlike the classical nSDBD, this coplanar configuration provides the overlapping of the discharge gap by conductive plasma channels. Generally, positive pulses are applied on the HV electrode coupled with negative DC components applied on the other exposed electrode, which demonstrated the ability to elongate the actuation region [14–17]. Bayoda et al. found that applying a negative DC voltage increases the input energy up to 300% and there existed a minimum potential difference between the two exposed electrodes at which the discharge gap of 40 mm can be overlapped [14]. Compared with a negative DC voltage, it is difficult to induce sliding discharges by applying a positive DC voltage [16]. Kourtzanidis et al. established a self-consistent model for a three-electrode nSDBD, with the third electrode powered by a negative DC voltage [18]. It is found that a negative streamer forms at the vicinity of the third electrode, and joins with the positive streamer from HV electrode.

The DC voltage can be replaced with a grounded electrode, which can also enhance the performance of SDBD [19–21]. In the experimental and numerical work of Peng et al., a transitional streamer phase is formed in the coplanar nSDBD with the third electrode grounded, which is characterised with random propagation and relative diffuse morphology [20]. In addition, the transition from streamer to spark transition in a three-electrode nSDBD powered by repetitive pulses was discussed. The memory effect of pre-heating and high densities of residual active species are essential in the formation of the streamer-to-spark transition [21].

The goal of this work is to offer experimental and numerical analysis of the thermal effect and hydrodynamic perturbation in a high-frequency pulse-periodic nanosecond coplanar surface dielectric barrier discharge (ncSDBD). Nowadays, there is no self-consistent experimental data on the thermal effect, ozone density and hydrodynamic perturbation in high-frequency (10–100 kHz) ncSDBD. With the two-dimensional model, the discharge morphology, fast gas heating, and hydrodynamic perturbations are analysed.

2 | Experimental Setup and Method

Coplanar nSDBD configuration is used in the experiments. In this configuration the high-voltage and low-voltage (LV) electrode which is grounded are both glued on the dielectric layer in the same plane. The schematic diagram of the electrode

system is presented in Figure 1a, which has a width (span) of 65 mm and an inter-electrode distance of 10 mm. The thin 0.3 mm Teflon dielectric layer (dielectric constant $\epsilon = 2.1$) was glued on the upper surface of Polyvinyl chloride (PVC). Both high voltage and imposed grounded electrodes are constructed from copper foil with a thickness of 50 μm . Imposed part of the grounded electrode is buried under the dielectric Teflon layer.

Positive polarity high-voltage pulses with a 10 ns pulse width at full width at half maxima (FWHM) and a 2 ns rise time are produced using a commercial pulser, FID Technology, FID30-100NM10X2. Four pulse repetition frequencies are considered in this work: 10, 20, 50 and 100 kHz. The voltage applied on the HV electrode is monitored with Tektronix PMK-14KVAC. As shown in Figure 1b, discharge current waveforms are measured using a current probe (Pearson model 6585), which is connected to the grounded electrode. The voltage and current signals are shown in Figure 2.

2.1 | Emission Spectroscopy

The emission spectra and temperature are obtained by emission spectroscopy technique. The optical emission, resolved both spatially and temporally, is collected with two quartz lenses (focal length $f = 100$ mm each). These lenses project the inter-electrode space on the entrance slit of the IsoPlane-320 monochromator (Princeton Instruments) with 1800 I/mm diffraction grating associated with the PI-MAX4 1024f intensified charge-coupled device (ICCD) camera, as shown in Figure 3a.

The spectra of selected molecular bands from the second positive system of molecular nitrogen, corresponding to the electronic transition $\text{N}_2(\text{C}_3\Pi_u) \rightarrow \text{N}_2(\text{B}_3\Pi_g)$, are analysed with respect to the number and repetition frequency of the pulses. The rotational and vibrational temperatures are determined by fitting the experimental spectra using SPECAIR software. To fit the experimental data, a slit function is measured experimentally using the Hg/Ar calibration lamp (Princeton Instruments).

To investigate the evolution of the discharge morphology, images are captured using a Pi-Max4 ICCD camera with a 105 mm, $f/4.5$ UV CoastalOpt SLR Lens. ICCD images, integrated over one pulse of the applied burst, are acquired using the 20 ns camera gate. The camera is externally triggered, with its signal synchronised to the initiation of the discharge.

2.2 | Ozone Absorption Spectroscopy

Figure 3b shows a diagram of the setup for the absorption measurement. The light source used is the 254 nm UV line emitted by a Hg-Xe lamp (OSRAM XBO 75 W/2 short-arc lamp). The UV light passes through the diaphragm and a plano-convex quartz lens ($f = 100$ mm), forming a parallel beam passing through the plasma region.

After the beam passes through the region of the ozone generation, a short-gated ICCD camera captures the beam pattern and

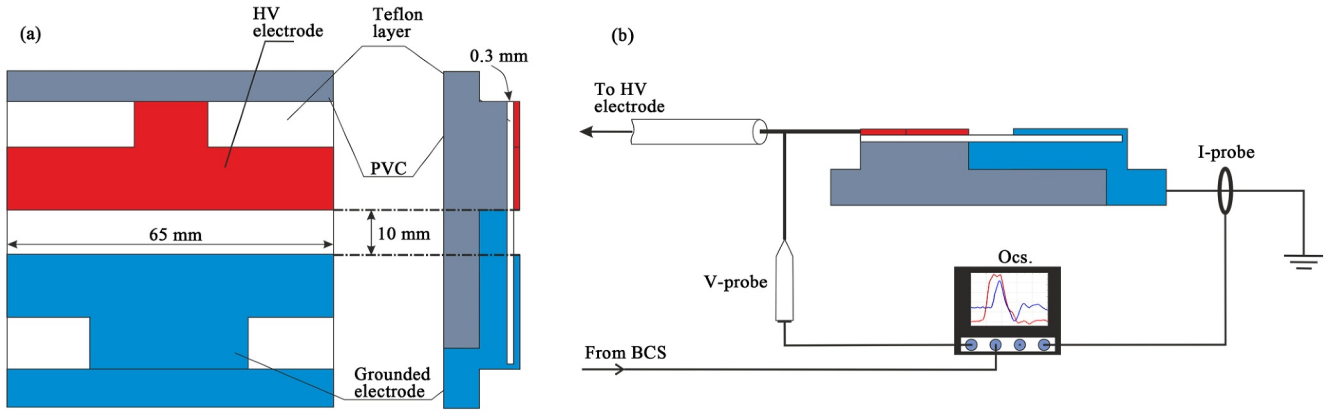


FIGURE 1 | The schematic diagram of the electrode system. (a) Front and side view; (b) voltage and current measurements.

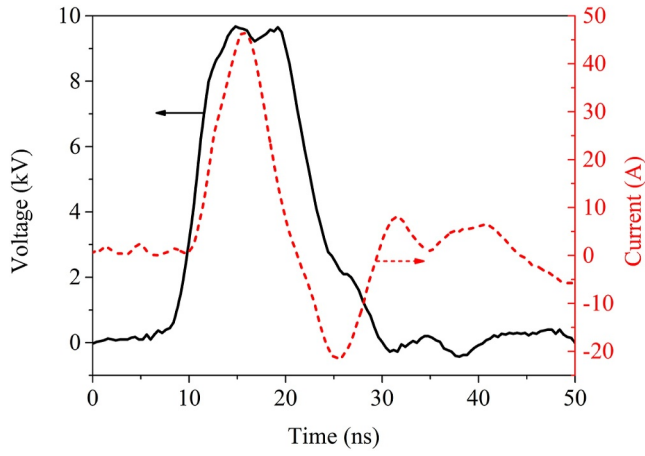


FIGURE 2 | Measured voltage and current waveforms.

then compared to a reference beam pattern, which is recorded without initiation of the discharge, in order to calculate the absorption ratio for each pixel. Then, the absolute ozone density is calculated for each pixel from the beam absorption ratio. The optical signals with and without plasma initiation are recorded with the Pi-MAX4 intensified camera quipped with a UV CoastalOpt SLR Lens associated with narrow band filter ((254 ± 5) nm Edmund Optics). Based on the Beer's law, the relationship between the ozone absorption and ozone number density distribution can be described as follows:

$$I = I_0 \exp\left(-\int_0^d \sigma N(x, y, z) dz\right) \quad (1)$$

where, d is the thickness of the ozone-occupied region, σ represents the absorption cross section of ozone, $N(x, y, z)$ denotes the ozone number density at any point in space (in cm^{-3}). I_0 and I are intensities of incident and transmitted light, respectively. The cross section of ozone absorption at 253.65 nm mercury line is $1.1329 \times 10^{-17} \text{ cm}^2$ [22]. Notably, the cross section of ozone absorption σ is temperature dependent, with a local UV maximum near 254 nm, decreasing by 15%–20% from 300 to 900 K. Additionally, the absorption at 254 nm has been confirmed in ref. [23] to be exclusively attributed to ozone for similar experimental conditions.

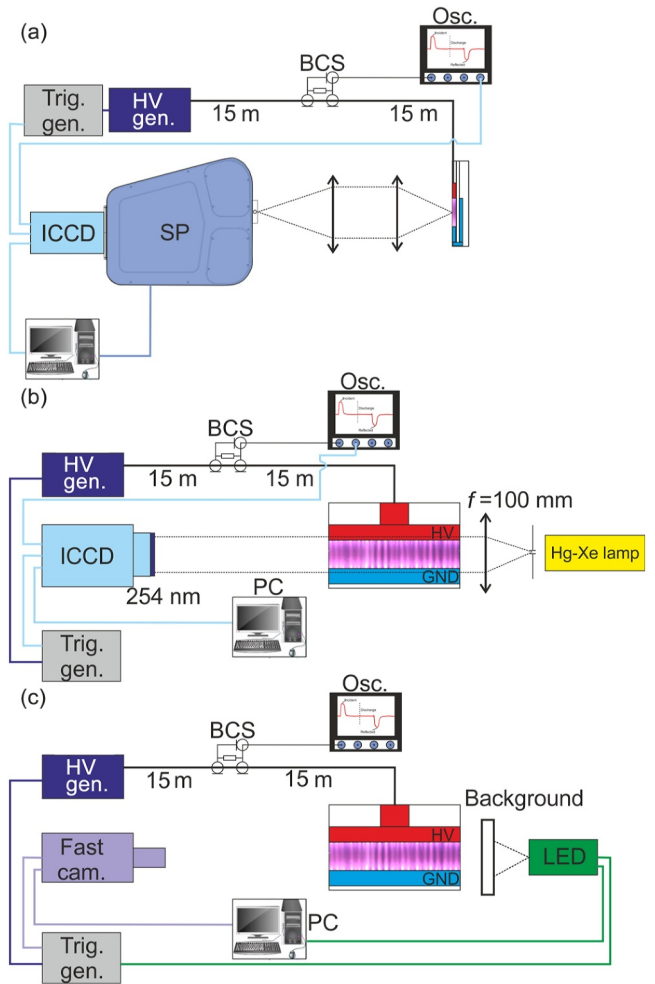


FIGURE 3 | Schematic of experimental facilities used for: (a) emission spectroscopy measurements; (b) ozone absorption measurements; (c) background-oriented schlieren.

2.3 | Background-Oriented Schlieren

The background oriented schlieren (BOS) method is used to visualise the refractive index perturbation. The relation between the refractive index and the gas density can be described by the Gladstone–Dale equation for gaseous media [24]. Due to the

refractive index perturbation induced by a schlieren object, a shift of the dotted pattern on the background plate behind the object will be observed. By assuming the symmetry along the line of sight direction, paraxial recording and small deflection angles, the relation between the refractive index and the displacement on the background can be written as follows [25]:

$$\nabla^2 n = \frac{n_0}{WZ_d} \nabla \cdot \mathbf{d}, \quad (2)$$

where n_0 is the refractive index of the surrounding gas, W is the width of the schlieren object in the line of sight direction, Z_d is the distance between the background plate and the schlieren object, and \mathbf{d} is the displacement vector of the dotted pattern on the background plane. Equation (2) is then discretised with a second-order finite-volume discretisation and solved in MATLAB.

The schematic of the set-up can be seen in Figure 3c. A dotted background pattern is pasted on a transparent plexiglass, which is illuminated by an LED (illuminator IL104). The background plate is placed 15 cm away from the centre of the electrodes. A high-speed camera (LaVision HighSpeedStar X) running at 10 kHz framing rate equipped with Nikon lens (AF Micro Nikkor 200 mm 1:4 D) is used to record the background pattern.

Fifty images without the presence of the discharge are first taken to get the average background image. Several pictures are then taken from the start of the discharge until 20 ms after the end of the discharge. These pictures together with the average background image are then post-processed with PIV algorithm in DAVIS software to infer the dotted pattern displacement. The displacement data are then evaluated in MATLAB to calculate the refractive index according to Equation (2).

3 | Model Description

The computational framework is established to resolve the discharge characteristic and the flow perturbation induced by repetitive pulses. Due to different timescales of the plasma discharge (nanosecond timescale) and flow response (microsecond timescale), these two stages are simulated separately. After the discharge stage, the FGH and body force are then incorporated into the hydrodynamic stage.

3.1 | Equations for the Discharge Stage

The numerical model for the discharge stage is based on 2D PASSKey (PARallel Streamer Solver with KinEtics) code. This code has been used and validated by comparison with measured discharge current, morphology, and streamer dynamics in modelling of nSDBDs [1, 10, 26, 27], pin-to-plane discharge [28] and discharges concerning streamer-to-spark transitions [29, 30]. More comprehensive details on the mathematical formulations, multiphysics and multiscale coupling strategies, as well as validations, are available in refs. [1, 26, 31]. Only a brief overview of equations is provided here.

The classical fluid model couples drift-diffusion-reaction equations, electron energy equation, Poisson's equation and Helmholtz equations for photoionisation, as given below:

$$\frac{\partial n_i}{\partial t} + \nabla \cdot \mathbf{\Gamma}_i = S_i + S_{ph}, \quad i = 1, 2, \dots, N_{total}, \quad (3)$$

$$\mathbf{\Gamma}_i = (q_i/|q_i|)\mu_i n_i \mathbf{E} - D_i \nabla n_i, \quad i = 1, 2, \dots, N_{ch}, \quad (4)$$

$$\frac{\partial}{\partial t}(n_e \epsilon_m) + \nabla \cdot \mathbf{\Gamma}_e = -|q_e| \cdot \mathbf{\Gamma}_e \cdot \mathbf{E} - P(\epsilon_m), \quad (5)$$

$$\mathbf{\Gamma}_e = -n_e \epsilon_m \mu_e \mathbf{E} - D_e \nabla (n_e \epsilon_m), \quad (6)$$

$$\nabla(\epsilon_0 \epsilon_r \nabla \Phi) = -\rho - \rho_c \delta_s, \quad (7)$$

$$\mathbf{E} = -\nabla \Phi, \quad (8)$$

$$\rho = \sum_{i=1}^{N_{ch}} q_i n_i, \quad (9)$$

$$\frac{\partial \rho_c}{\partial t} = \sum_{j=1}^{N_{ch}} q_j (-\nabla \cdot \mathbf{\Gamma}_j), \quad (10)$$

where n_i , $\mathbf{\Gamma}_i$, q_i , μ_i and D_i represent the number density, flux, charge, mobility and diffusion coefficients for each species i , respectively. S_i represents the source term, which is obtained by solving detailed reaction kinetics. N_{ch} and N_{total} are the number density of charged species and all species, respectively. The photoionisation source term S_{ph} is calculated via three-exponential Helmholtz equations, the parameters of Helmholtz equations for air have been given in ref. [32]. n_e , $\mathbf{\Gamma}_e$, and q_e are electron density, electron flux and elementary charge, respectively. D_e , μ_e , $\mathbf{\Gamma}_e$ and ϵ_m are electron energy diffusion, electron energy mobility, electron energy flux and the mean electron energy, respectively. The rate coefficients of electron impact reactions and electron swarm coefficients are expressed as a function of ϵ_m [33]. The ion mobility and diffusion coefficients are obtained from experimental data [34] and calculated using MOBION package [35]. $P(\epsilon_m)$ denotes the power loss in electron collision reactions, calculated using BOLSIG+ [33, 36, 37]. The electric field is represented by \mathbf{E} , and the electric potential by Φ . ϵ_0 and ϵ_r stands for the vacuum permittivity and relative permittivity, respectively. ρ and ρ_c refers to the density of space charge and surface charge, respectively. δ_s denotes the Kronecker delta function, which equals to 1 on the plasma/dielectric interfaces.

The three-exponential Helmholtz equations can be expressed as follows:

$$S_{ph}(\mathbf{r}) = \sum_j S_{ph}(\mathbf{r}), \quad (11)$$

$$\nabla^2 S_{ph}(\mathbf{r}) - (\lambda_j p)^2 S_{ph}(\mathbf{r}) = -A_j p^2 \frac{P_q}{p + P_q} \mathbf{I}(\mathbf{r}), \quad (12)$$

$$\frac{\Psi_0(\mathbf{r})}{p} = (pr) \sum_j A_j e^{-\lambda_j pr} \quad (13)$$

$$\frac{\Psi_0(\mathbf{r})}{p} = \frac{1}{4\pi} \frac{\omega}{\alpha_{eff}} \frac{\int_{\lambda_{min}}^{\lambda_{max}} \xi_\lambda(\mu_\lambda/p) \exp(-\mu_\lambda/p) pr I_\lambda^0 d\lambda}{\int_{\lambda_{min}}^{\lambda_{max}} I_\lambda^0 d\lambda}, \quad (14)$$

where $S_{ph}(\mathbf{r})$ is the photoionisation source term at position \mathbf{r} , λ_j and A_j ($j = 1, 2, 3$) are fitting parameters for Equation (12), p_q is the quenching pressure of the emitting gas, p is the gas pressure, $I(\mathbf{r})$ is the ionisation source rate, $\Psi_0(\mathbf{r})/p$ is the photoionisation functions, ω is the excitation coefficient of emitting states, α_{eff} is the effective Townsend coefficient, $(\lambda_{min}, \lambda_{max})$ is the spectral range of the radiation, ξ_λ and μ_λ are the spectrally resolved photoionisation yield and the absorption coefficient, respectively, and I_λ^0 is the spectral density of ionising radiation.

The kinetics scheme in ref. [10] is employed in this model. This kinetics can effectively describe the streamer dynamics and FGH [1, 26, 27, 31, 38], but it has not been proven to be enough to resolve SDBD phenomena including filament transition. The reason for using this kinetics is to investigate the streamer propagation and hydrodynamic perturbation for 10 kHz, where the morphology has a quasi-uniform structure (discussed later). The modelling of the transition to filament is outside the scope of this model. The main species of the reaction system are: e (electron), N_2 , O_2 , $N_2(A_3\Sigma_u^+)$, $N_2(B^3\Pi_g)$, $N_2(C^3\Pi_u)$, N_2^+ , N_4^+ , $O_2^+N_2$, O^- , O_2^- , O_2^+ , O_4^+ , O , $O(^1D)$. The scheme includes in total 15 species and 38 reactions.

3.2 | Equations for the Flow Perturbation Stage

The gas dynamics is solved by the commercial software COMSOL Multiphysics based on the compressible Navier–Stokes equations. The equations are given below:

$$\frac{\partial \rho}{\partial t} + \nabla \cdot (\rho \mathbf{u}) = 0, \quad (15)$$

$$\frac{\partial \rho \mathbf{u}}{\partial t} + \rho \mathbf{u} \cdot \nabla \mathbf{u} = -\nabla p + \nabla \cdot [\mu(\nabla \mathbf{u}) + (\nabla \mathbf{u})^T] + \mathbf{f}_b, \quad (16)$$

$$\mathbf{f}_b = q_e(n_p - n_n - n_n)\mathbf{E}, \quad (17)$$

$$\rho C_p \mathbf{u} \cdot \nabla T - \nabla \cdot (k \nabla T) = \sum_j R_j \varepsilon_j. \quad (18)$$

In the above equations, ρ , \mathbf{u} , p and μ represent the neutral gas density, velocity, pressure and viscosity of the fluid, respectively. The coupling term \mathbf{f}_b is the body force, which is mainly a Coulomb force. n_p , n_n and \mathbf{E} are positive ions density, negative ions density and electric field, respectively. C_p , T and k represent specific heat capacity, gas temperature and thermal conductivity, respectively. The heating term $\sum_j R_j \varepsilon_j$ includes different exothermic reactions for the increase in gas temperature. R_j and ε_j are the reaction rate and energy release of the j th reaction [10], respectively.

3.3 | Domain, Mesh, Initial and Boundary Conditions

Figure 4 shows the computational geometry with a domain of $3 \text{ cm} \times 3 \text{ cm}$. Both the high-voltage electrode and the exposed grounded electrode have a length of 10 mm and a thickness of $50 \mu\text{m}$, forming a discharge gap of 10 mm. Another grounded electrode is located at $y = 0$ position, measuring 20 mm in length

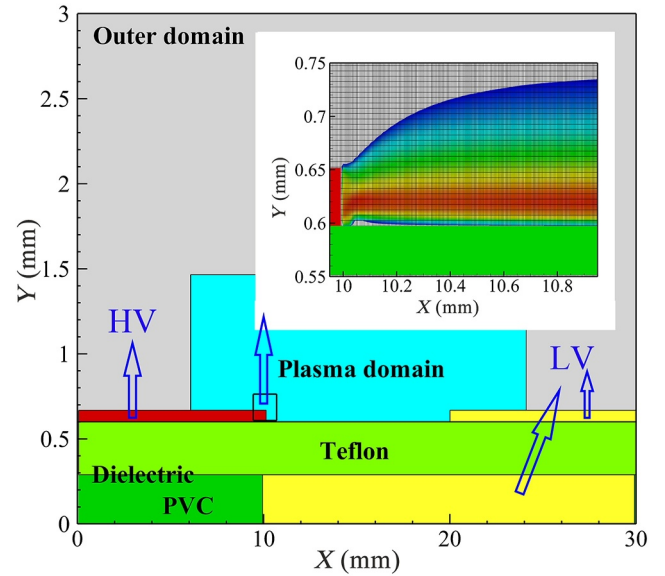


FIGURE 4 | Geometry and mesh distribution. Bright blue domain: plasma region; red domain: high-voltage electrode; green domain: dielectric; yellow domain: grounded electrodes.

and 0.3 mm in thickness. The barrier dielectric is made of PVC ($\varepsilon_{PVC} = 4$) and Teflon ($\varepsilon_{Teflon} = 2.1$) flat plate with the thickness of 0.3 mm. The simulated condition is 1 bar pressure and 300 K. The plasma domain is assigned a uniform mesh size of $5 \mu\text{m}$, and outside this domain, the mesh size expands exponentially. The total number of grids is about 0.5 million, with 0.33 million allocated to the plasma region.

The initial electron density is set to a uniform value of 10^{10} m^{-3} , and the initial densities of ions are determined based on quasi-neutrality. The initial mean electron energy is set as 0.5 eV. Detailed descriptions of the boundary conditions can be found in ref. [31].

For the flow perturbation phase calculation, the domain is extended up to $200 \text{ mm} \times 200 \text{ mm}$ to evacuate properly the pressure wave generated by the discharge. To save the computational costs, a non-uniform structured mesh of 800×200 is employed. To resolve the fine flow features, the mesh is locally refined in the discharge region and boundary layer with the smallest cells being $2 \mu\text{m}$ square. The adiabatic nonslip walls are used on the electrode and dielectric surfaces, ignoring the heat conduction through them.

4 | Experimental Results and Discussion

4.1 | Emission Spectroscopy of the ncSDBD

Four PRFs are considered: 10, 20, 50 and 100 kHz. In all cases, the number of pulses in the applied burst is set to the same 500 pulses. Figure 5 shows the ICCD images of the 1st, 100th and 500th pulses. The discharge emission was integrated over the discharge phase and early afterglow with the camera gate of 100 ns. For 10 kHz, the morphology has a quasi-uniform

structure. Although the pulse number and pulse repetition frequency increase, the discharge becomes more filamentary.

It is important to distinguish the contraction of the ncSDBD from the filamentary regime of the nSDBD that was studied experimentally before [2]. The filamentary regime of the nSDBD takes place within a single pulse regime at elevated pressures and propagates for a significantly longer distance from the edge of HV electrode. The streamer-to-filament transition in a single pulse was studied over a wide range of pressures (3–6 bar) and voltage amplitudes (30–60 kV) on the high voltage electrode [39]. The rise rate for the voltage can reach 15–30 kV/ns, and the total energy deposited into discharge is equal to 49 mJ in the case of the filamentary discharge at 6 bar and 50 kV. In our case, the voltage rise rate is about 2 kV/ns, and the total deposited energy is about 2.2 mJ. This filament regime was used for increasing the ignition efficiency of ultra-lean H_2 /air combustible mixtures at elevated pressures [40]. Later, it was shown that this regime leads to the plasma in local thermal equilibrium (LTE). The electron density in filaments reaches the value of 10^{19} cm^{-3} [3, 39]. Stepwise ionisation mechanism was proposed to explain the rapid transition to the LTE regime in ref. [3]. Meanwhile, the similar plasma regime was observed in open-electrode pin-to-pin nanosecond spark discharge in atmospheric air [41]. Later it was found that the key role in extremely fast ionisation is played by ionisation from excited states of atomic nitrogen [42, 43].

The main characteristic feature of such a regime is a sharp change in the emission spectrum from the second positive system of molecular nitrogen to a broadband emission with intense emission lines of N^+ and O^+ ions. In the present study, neither broadband emission nor emission lines of ions are observed in the emission spectra in all experimental conditions.

The filamentary structure with the increase in pulse number and repetition frequency may be explained by saturation or non-uniform distribution of the surface charge caused by the previous pulse, which was proposed in [44]: the saturation effect, which occurs when the screening effects of surface charge and space charge are comparable, can disrupt the spatial uniformity of the discharge.

In order to understand the dynamics of the heat release, the spatially and temporally resolved measurements of the emission spectroscopy were conducted. The interelectrode gap (10 mm) is projected on the entrance slit of the spectrometer. The resulting 2D emission spectra are split into 10 sections integrating the

optical emission every millimetre of the discharge gap. Emission spectra are acquired for four considered frequencies of the applied pulses and are obtained for 1st, 100th, 200th, 300th, 400th and 500th pulses. The results of temperature measurements are shown in Figure 6.

It can be seen that for 10 kHz frequency practically no gas heating occurs throughout the entire length of the discharge gap. The total temperature increase does not exceed 50 K. With increase in the pulse repetition frequency and number of pulses, the gas temperature in the plasma region gradually increases. For 20, 50 and 100 kHz, the mean temperatures along the discharge region during the 500th pulse are equal to (470 ± 10) , (560 ± 10) and (690 ± 10) K, respectively.

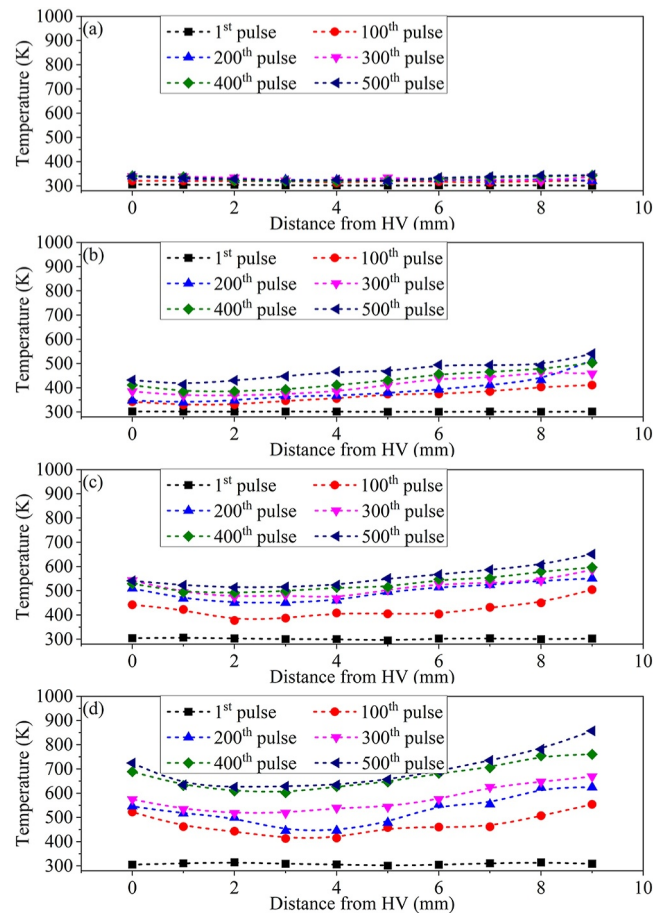


FIGURE 6 | Spatial profile of the temperature measured for (a) 10 kHz, (b) 20 kHz, (c) 50 kHz, (d) 100 kHz.

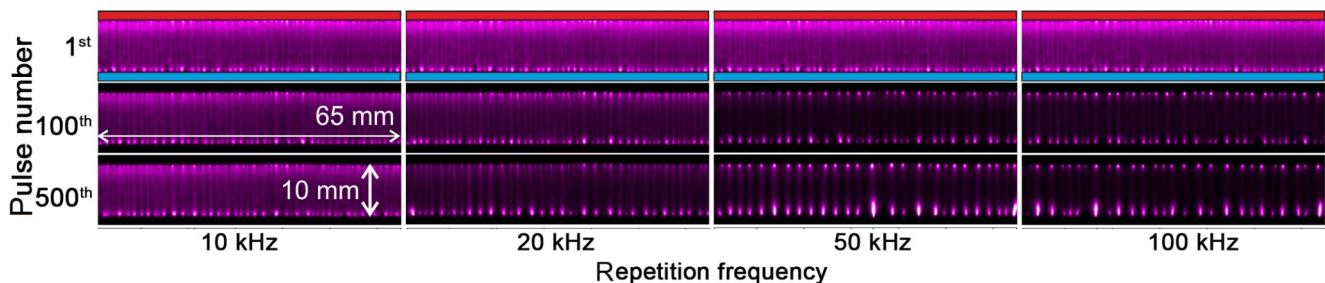


FIGURE 5 | ICCD images of the discharge for different pulse repetition frequency and pulse numbers.

The temperature distribution along the plasma channels is also a function of PRF. For 20 kHz, the temperature monotonically decreases with increase of the distance from the grounded electrode, and slightly increases near HV electrode. Although increasing the PRF, the minimum of temperature distribution moves towards the centre of the discharge gap. The highest temperature is always observed near the grounded electrode that serves as a cathode for positive polarity discharge.

4.2 | Spatial Distribution of Ozone Density

Figure 7 shows the ozone density distribution right after the discharge burst containing 500 pulses and 10 ms after the last pulse. It should be noted that by changing the PRF, the absolute time of plasma actuation is also altered. For 10 kHz frequency, the actuation time is 50 ms; for 100 kHz it is only 5 ms right after the 500th pulse. The spatial distribution of ozone density is defined by kinetics, diffusion and convection away from the discharge region. Therefore, we operate with a relative delay (RD) while considering the behaviour of the discharge afterglow, which is a delay after the last pulse.

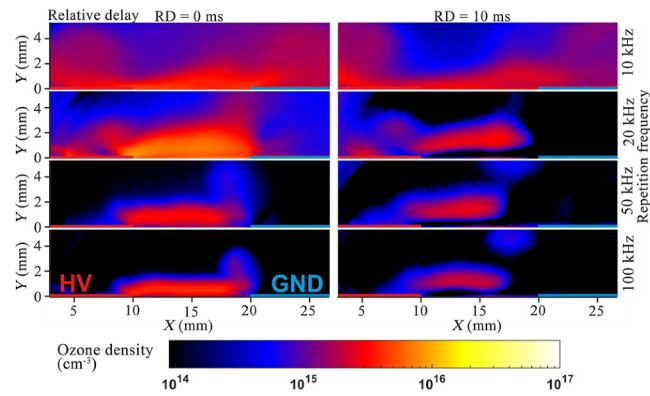


FIGURE 7 | Ozone density distribution right after the 500th pulse (left column) and 10 ms after the 500th pulse (right column). All absorption profiles were obtained with 10 μ s camera gate and averaged over 500 frames.

It can be seen in Figure 7 (RD = 0 ms) in the early afterglow period ($t < 1 \mu$ s) that the ozone is generated on the surface and in the volume above the electrode system. The high ozone density region is observed in the vicinity of the dielectric surface for all considered PRFs. The volume occupied by ozone and absolute density are highest for 20 kHz. The volume of high ozone density for RD = 0 ms is observed both for 10 and 20 kHz. For higher frequencies, the ozone density decreases and the regions of the ozone density are concentrated in a layer of about 2 mm thickness above the dielectric surface.

The ozone decay rate increases exponentially with an increase in the gas temperature [45]. Figure 7 (RD = 10 ms) shows the ozone distribution 10 ms after the last pulse. At 10 kHz the shape of the ozone density field does not change significantly, whereas, at higher frequencies, the effective volume occupied by ozone and the absolute value of ozone density decrease. As it was mentioned above for PRF = 10 kHz, there is no noticeable gas heating. The lower gas temperature in the vicinity of the dielectric surface leads to the fact that the high ozone signal remains attached to the surface saving the high absolute density values even 10 ms after the discharge. For higher PRFs, the gap with lower ozone signal can be observed near the surface. This is because the gas temperature increases with increase of PRF. As it was mentioned in Section 4.1, the highest gas temperature is observed near the grounded electrode. This contributes to the fast decay of ozone near the grounded electrode. Thus, the amount and dynamics of ozone density are largely determined by the frequency of the applied pulses.

4.3 | Background-Oriented Schlieren Measurements

Figure 8 demonstrates the scalar field of refractive index values and the vector field of its gradient for different time moments in the post-discharge period for different PRFs. The colour scale of each BOS image is scaled with respect to their minimum and maximum values. It should be noted that the field of view of the BOS images is set to start from 1.1 mm above the dielectric surface in order to eliminate the computational noise at the boundary close to the surface and exposed electrodes.

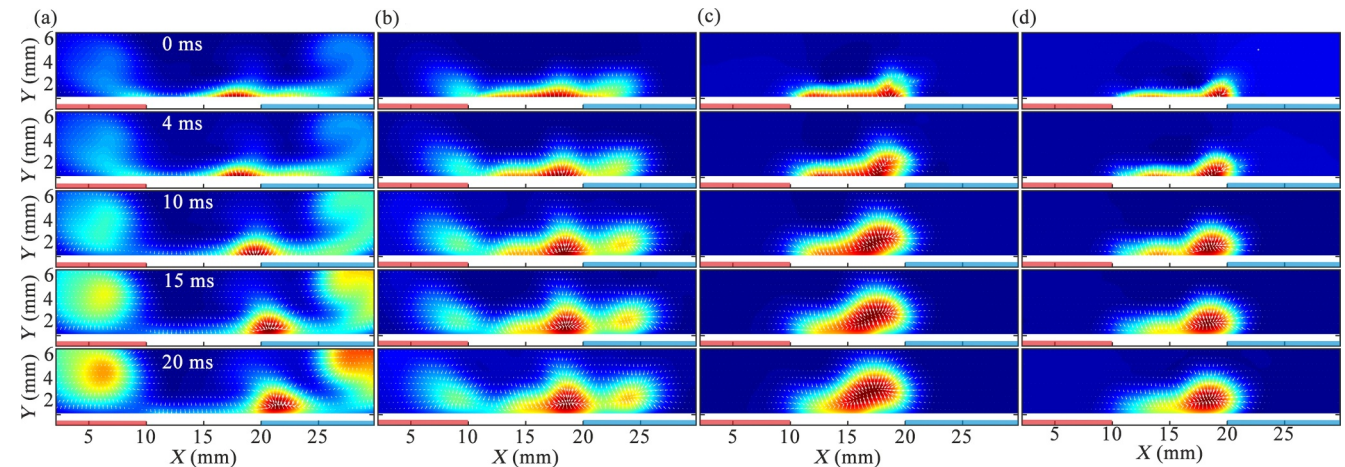


FIGURE 8 | BOS images of the discharge afterglow at different time moments (0–20 ms) for (a) 10 kHz, (b) 20 kHz, (c) 50 kHz and (d) 100 kHz.

The schlieren image depicts a change in density, which may be related to the temperature change caused by the energy released by the plasma actuator. The heated gas undergoes thermal expansion after the discharge. For the case of 10 kHz, 0–4 ms after the discharge, an up-blowing flow fluctuation like a vortex structure is observed near the two exposed electrodes.

At later time instances and frequency above 20 kHz, the region of high refractive index values propagates upwards. Furthermore, high refractive index values exist in the region close to the grounded electrode. The cause of the deviation and upward movement deserves more experimental and numerical investigation.

5 | Results of Plasma Modelling

The experimental data of the electric current is selected as a benchmark to confirm the validity of this model. The direct comparison is shown in Figure 9. The temporal evolution of the calculated current shows a qualitative agreement with the

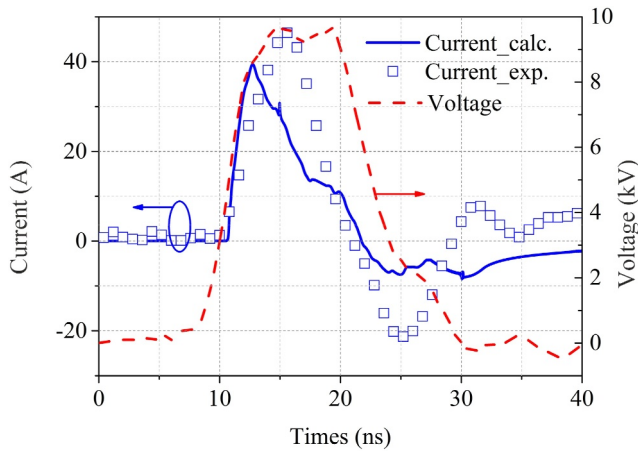


FIGURE 9 | The calculated and experimental current.

measured data. The current waveform shows positive and negative peaks, although the negative peak value is significantly lower than the positive one. The positive current corresponds to the rising phase and the initial falling phase of the applied voltage, indicating the formation of the ‘forward breakdown’ surface ionisation wave. During the latter falling phase, the current reverses its direction, resulting in the ‘reverse breakdown’ ionisation wave [46, 47].

5.1 | Discharge Evolution

Figure 10 plots the electron density and reduced electric field at 14, 20, 29 and 30 ns. Similar to classic nSDBD, streamers initiate from the HV electrode and are ionised by the high electric field strength at the discharge front [48]. The streamer propagates above the dielectric surface, leaving a discharge channel with low electric field strength, which is always lower than the ionisation threshold for air ($(E/N)_{\text{thre}} = 120$ Td). During propagation, the thickness of the positive streamer remains nearly constant, about 69 μm , which is consistent with the analytical results presented in ref. [49]:

$$h_d = 65.9/p, \quad (19)$$

where h_d (μm) is the surface streamer thickness, which is dependent on pressure p (bar).

With the streamer propagation towards the grounded electrode, a large amount of positive charge accumulates at the streamer head, which can be regarded as a virtual anode. At 29 ns, the streamer head is very close to the grounded electrode, forming a high electric field between the streamer head and grounded electrode, and increased ionisation takes place. This local-enhanced ionisation causes a ‘corona-like’ discharge at the grounded electrode. At 30 ns, the streamer merges with the ‘corona-like’ cloud, and the inter-electrode gap is overlapped by the streamer. The intensified ionisation contributes to more

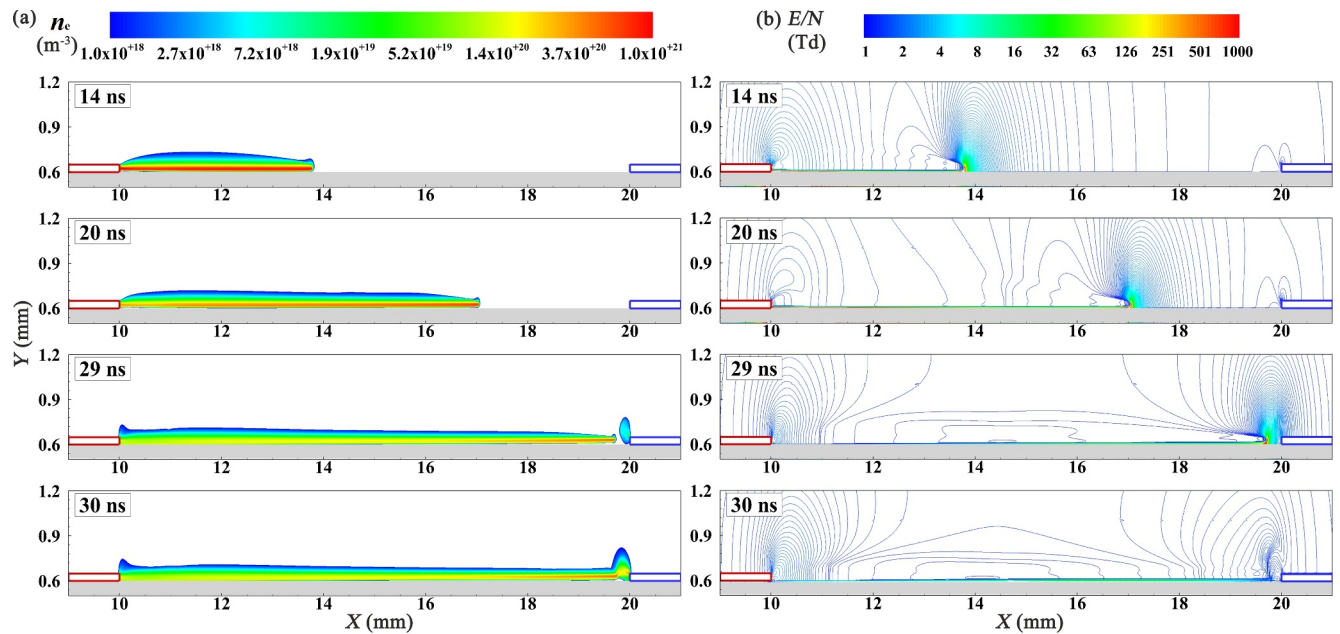


FIGURE 10 | Evolution of (a) electron density and (b) reduced electric field strength for different time instants.

generation of electrons at the tip of grounded electrode. Experimental results also revealed that a brighter luminous discharge occurs at the exposed grounded electrode when the discharge gap is overlapped [14, 20].

In the classic SDBD geometry, the propagation length l_{\max} of positive streamers is derived analytically in a recent work [50].

$$l_{\max} \approx \frac{2h_d \nu_{ic} V_{\text{peak}}}{\mu_e E_c^2}, \quad (20)$$

where h_d is 69 μm mentioned before. $\nu_{ic} = 3.5 \times 10^{11} \text{ s}^{-1}$ is the reduced ionisation frequency, $\mu_e = 600 \text{ m}^2/\text{V/s}$ is the electron mobility and $E_c = 277 \text{ kV/cm}$ for an atmospheric surface streamer. Here, the peak voltage is 10 kV, corresponding to the $l_{\max} \approx 10.5 \text{ mm}$. If the simulation is conducted in the classic SDBD geometry (just to remove the exposed grounded electrode) under the same conditions, the streamer length is about 10.7 mm, which is close to the analytical result. This indicates that even without the presence of the exposed grounded electrode, the streamer can still cover the entire length of 10 mm. An interesting question is if the length of the streamer in classic SDBD geometry (without the exposed grounded electrode) is less than the gap distance, will it overlap the entire gap with the help of the grounded electrode?

The streamer evolutions at different time instants in cases of 8.5, 9.0 and 9.5 kV are presented in Figure 11. In classic SDBD calculations, the maximum propagation lengths for these three cases are 9.1, 9.7 and 10.2 mm, respectively (the results are not shown here). In ncSDBD geometry, the streamer in 8.5 kV finally stops at 9.1 mm away from HV electrode and failed to overlap the gap. This indicates that the exposed grounded electrode has little effect on the streamer propagation. In the cases of 9.0 and 9.5 kV, when the streamers reach approximately 9.6 mm from HV electrode, negative discharge is formed with an electron increase at the tip of grounded electrode. This is because the potential at the positive streamer head creates a strong electric field between the streamer head and grounded electrode. This ‘corona-like’ streamer connects with the positive streamer at a speed of about 0.1 mm/ns, like a bridge. In the case of 9.5 kV, after 34 ns, the positive streamer propagates towards the grounded electrode through the pre-ionised channel created by the negative discharge. Though the propagation length for the positive streamer in 9.0 kV is shorter than the gap distance, the existence of the grounded electrode ‘helps’ to overlap the gap.

5.2 | Hydrodynamic Perturbation

According to the ozone distribution and BOS images, in the case of 10 kHz, the flow field blows up above two exposed electrodes right after 500 pulses. To explain the flow pattern above the exposed electrodes in repetitive discharges, a numerical simulation is conducted. The discharge stage and the flow response are simulated separately. In order to save computational costs, the discharge process is only calculated up to 1000 ns. Due to the longer time scale of the flow response, the time-averaged body force and FGH energy derived from the discharge calculation is used as an input into COMSOL to solve Navier–Stokes equations. For 10 kHz, the discharge morphology keeps quasi-uniform and almost no gas heating occurs with the increase of pulse number. An important assumption here is that individual pulses behave as a single-pulse case (independent of each other), so the momentum/energy input can be seen as the same during each period.

For sinusoidal voltages, the airflow disturbance is induced by body force. According to the results of Little et al. [51] and Starikovskii et al. [7], the momentum input into the flow by nSDBD is so weak that it can be ignored. The local fast gas heating is recognised as the main physical mechanism for hydrodynamic perturbation of nanosecond SDBD. Numerical results demonstrate that the shock wave induced by FGH produces transient local perturbation [52–55]. The change in flow pattern located in the discharge zone is always the study subject, and no obvious vortex upstreaming moving was found above the HV electrode. A reverse flow towards upstream was observed experimentally above the exposed electrode, which is supposed to be generated during the voltage falling phase [56]. To elucidate the efficacy of pulse-periodic ncSDBD for flow perturbation, the effect of FGH and body force will be studied separately.

The simulation starts by examining the effect of FGH. Contours of temperature, pressure and velocity perturbation during the first period are shown in Figure 12. Figure 12a shows the temperature distribution at 40 ns. The temperature rise is observed near electrodes and above the dielectric surface. The temperature reaches its maximum of 345 K near the edge of high-voltage electrode. In reality, the wall boundaries must be heated. The heat loss rate of the wall to ambient or to mounting material determines the cooling rate, which would balance the energy gain of the wall. In order to simplify the model, the adiabatic nonslip walls are considered on the electrode and dielectric surfaces.

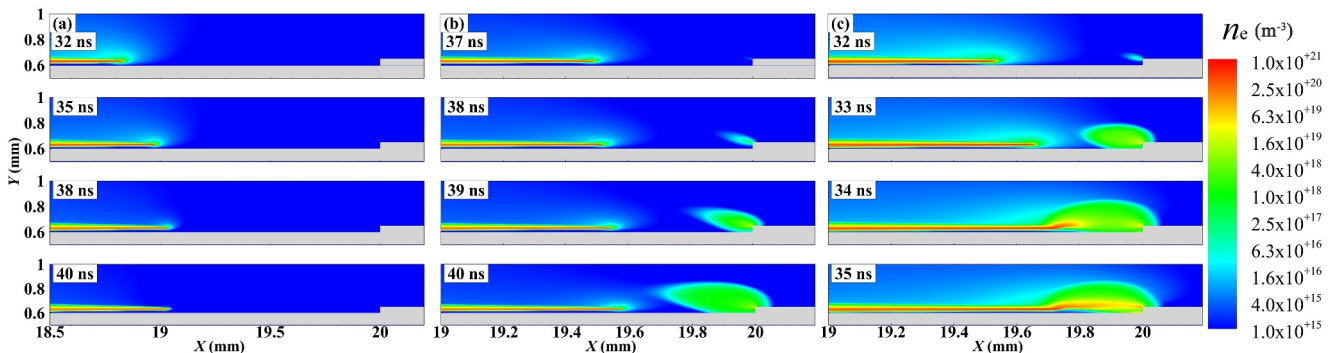


FIGURE 11 | Distribution of electron density for (a) 8.5 kV, (b) 9.0 kV, and (c) 9.5 kV at different time points.

It should be underlined that the simulation was performed for a single discharge. The first row of the ICCD images of the discharge shown in Figure 5 shows the first discharge pulses. The intensity of the discharge is mostly dominated by emission of the second positive system of molecular nitrogen. The excitation of the $N_2(C_3\Pi_u)$ state during the nanosecond discharges occurs by means of direct electron impact. Therefore, the emission intensity of the discharge is indirectly dictated by the local energy deposition. It can be clearly seen that in all images of the first pulses, the highest emission intensity is observed near the HV electrode. This is because the exposure time of the camera integrates the emission of the discharge during one applied pulse. Therefore, it can be assumed that the specific deposited energy is higher near the HV electrode. Under repetitive pulses, the highest temperature occurring at the grounded electrode may be explained as follows: when the discharge gap is covered, secondary emission and field emission at the cathode surface increase the electron density near the cathode, leading to more fast gas heating.

Figure 12b shows the shockwave structure, consisting of two semispherical waves at the edge of exposed electrodes and a planar wave, as observed in ref. [15]. The pressure gradient of

the semi-spherical region at LV electrode is weak due to the smaller temperature rise. The localised perturbation induced by the shock wave is limited in a narrow region behind its front. It can be seen that the shock wave is followed by a rarefaction wave, which keeps some distance behind the shock.

Figure 12c shows the velocity distribution at the end of the first period 100 μ s. With the propagation of shock waves, the localised velocity fluctuation behind the shock front decays quickly to the static state, exhibiting transient nature. Notably, the fluctuation near the HV electrode becomes more pronounced, which manifests its presence as a pair of counter-rotating vortices, as illustrated in Figure 12d. Just as found in ref. [57], this slow perturbation, different from the former compression wave (time scale $\sim 1\text{--}10$ μ s) is generated on a long time scale (> 100 μ s). The origin of this perturbation is explained as a combination effect of shock wave and residual heat [55].

The subsequent development of velocity at the end of 2nd, 5th and 10th period is shown in Figure 13. The perturbation near HV electrode gradually becomes stronger as the pulse number increases. However, from the numerical results, the perturbation caused by FGH cannot explain the experimental

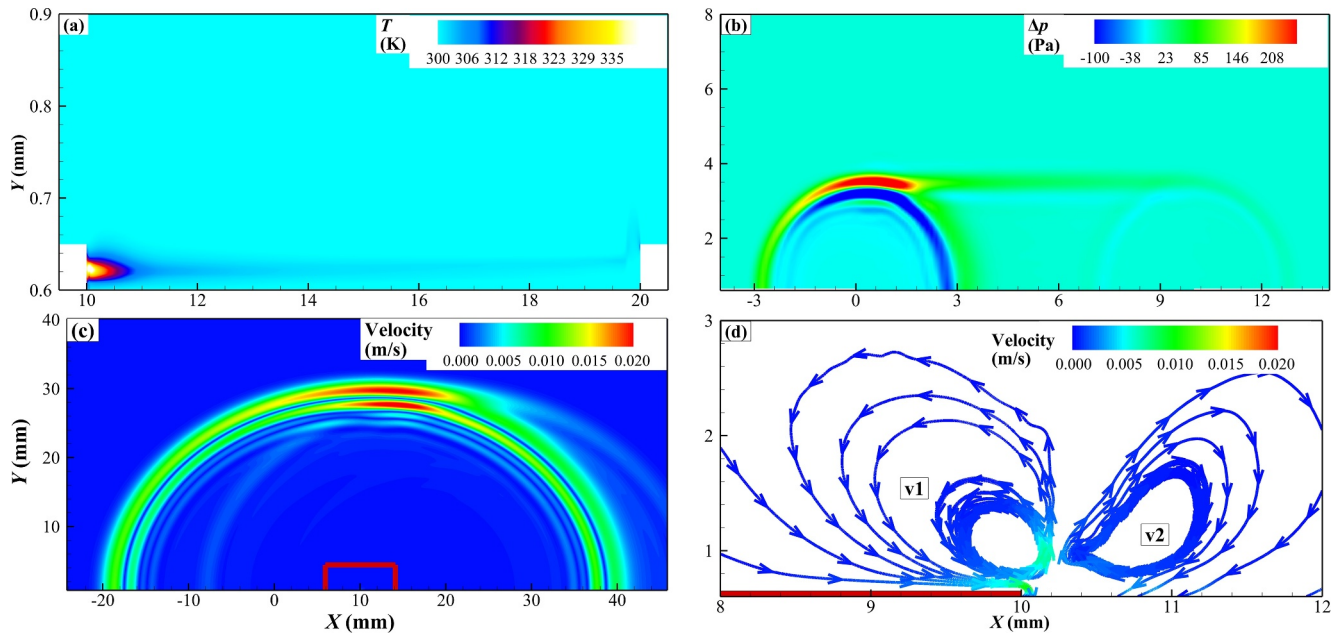


FIGURE 12 | Contours of hydrodynamic perturbation: (a) temperature distribution at 40 ns; (b) pressure perturbation Δp at 10 μ s; (c) velocity fluctuation at the end of the first period 100 μ s; (d) the zoom of the region marked by the red line in (c). v1 and v2 denote two counter-rotating vortices.

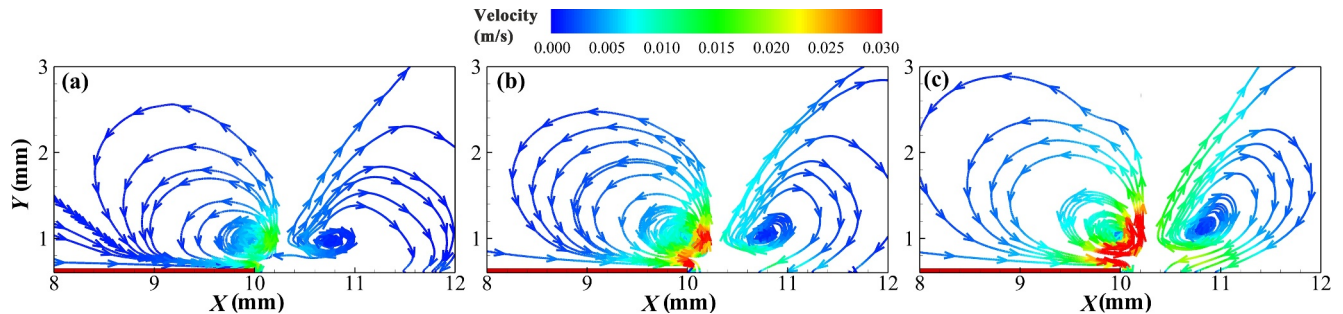


FIGURE 13 | Streamlines of velocity fluctuation fields at the end of (a) 2nd (0.2 ms), (b) 5th (0.5 ms) and (c) 10th (1 ms) period, respectively.

phenomenon. The vortex at the tip of HV electrode is counterclockwise; therefore, it is impossible to blow the gas up to the left.

Then, the effect of the body force is discussed. In order to save computational costs, the discharge process is only calculated up to 1000 ns. The time-averaged force is used as an input and applied repeatedly for 500 cycles. The body force is determined by the density of the space charge and the electric field, mainly located in the streamer head and/or near-electrode region [57].

In the positive streamer phase, the positive ion cloud expands over the dielectric surface. The streamer head is positively charged and the electric field is high, where the body force is positive in the x -direction [58]. Due to the short time scale of this phase, the momentum input to the flow is small.

The time scale of the relaxation process ($t \geq 40$ ns) is longer than that of the positive streamer phase. Figure 14 shows the distribution of the space charge density, electric field and body force

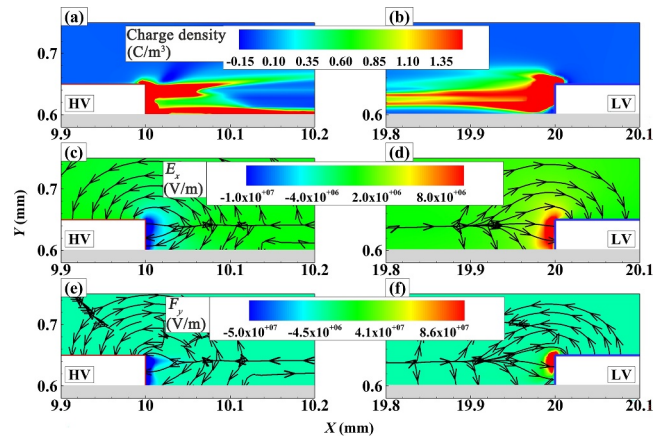


FIGURE 14 | Distributions of the space charge density ((a) near HV, (b) near LV), x -component of the electric field E_x ((c) near HV, (d) near LV) and x -component of the body force F_x ((e) near HV, (f) near LV) at 600 ns.

at 600 ns. In this relaxation phase, the cathode layer formed near the electrode has a strong electric field [48], causing a large number of positive charges to accumulate nearby under the effect of charge separation (shown in Figure 14a,b). A modelling investigation on the influence of surface charge in nSDBDs reported that, during the voltage falling phase, E_x near the high-voltage electrode reverses its polarity [59]. The negative and positive E_x regions are generated near the HV and LV electrode, respectively (shown in Figure 14c,d). This electric field pulls this positively charged layer progressively further until it is quenched, and this relaxation process is slow [58]. The body force (shown in Figure 14e,f) is strongly negative and x -directed in the vicinity of the HV electrode (positive and x -directed in the vicinity of the LV electrode).

Figure 15 depicts the development of the perturbation right after 1st, 100th, 300th and 500th pulses. A 'starting vortex' is generated with circulation in the clockwise/counterclockwise direction at the tip of the HV/LV electrode. The velocity reaches its maximum near the electrode tip. With the increase of pulse number, the vortices convect away from the discharge gap. It is a result of the accumulating effect of momentum input by multiple pulse, just like the experimental phenomenon. Compared with the experimental results, the perturbation region is limited in volume after 500th pulses. It should be noted that the momentum input considered only within 1000 ns in one period is definitely lower than it actually is, so the calculated velocity will be lower. Despite the discrepancy, numerical results can lead to the conclusion that the body force triggers the blowing up of the flow.

6 | Conclusion

An experimental and numerical study of positive polarity nano-second pulsed surface dielectric barrier discharge in coplanar arrangement is carried out. The thermal effect, absolute ozone density, and flow perturbation are measured by means of emission spectroscopy, spatially resolved absorption and background-oriented schlieren. The direct imaging of the discharge with a short camera gate is used for analysis of discharge morphology. It

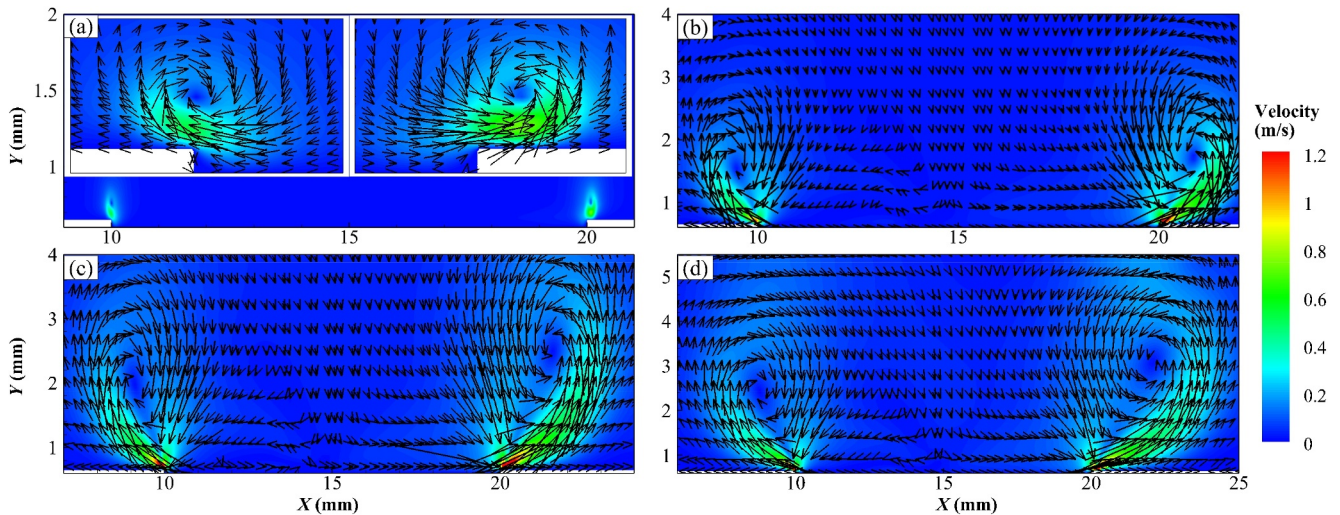


FIGURE 15 | Flow perturbation right after the (a) 1st, (b) 100th, (c) 300th and (d) 500th pulse.

is shown that quasi-uniform streamer discharge becomes filamentary with an increase in discharge frequency and the pulse number, and the high intensity region occupies the area in the vicinity of both the HV and ground electrodes.

Spatially resolved temperature measurements show that the mean temperature increases from (340 ± 10) K to (690 ± 10) K while increasing the pulse periodic frequency from 10 to 100 kHz. The highest value of heat release is observed in the cathode region near the grounded electrode. Absolute ozone density measurements show that the amount of ozone changes significantly with different PRFs. The volume occupied by ozone and absolute density are highest for PRF = 20 kHz and decreases at higher frequencies.

The discharge characteristics and hydrodynamic perturbations are numerically studied. The discharge morphology shows that when the positive streamer propagates close to the exposed grounded electrode, a negative discharge is formed in the vicinity of LV electrode, which merges with the positive streamer overlapping the entire discharge gap. Two semi-spherical waves with a planar wave are generated from the fast gas heating and propagate away from the discharge region, leaving a pair of counter-rotating vortexes. During the relaxation phase, a large amount of positive charges accumulate nearby under the effect of charge separation, and the strong body force is generated near two exposed electrodes. The vortex is generated with circulation in the clockwise/counterclockwise direction at the tip of the HV/LV electrode, blowing up of flow.

Multiphysics modelling of nSDBD of atmospheric gas is challenging work due to the coupling between discharge and hydrodynamic phase. Especially in repetitive pulsed discharge, the temperature rising and flow perturbation caused by the deposited energy and momentum input with increasing pulse number, will inevitably affect the next pulse characteristics. Here, just for simplicity of calculation, we ignore the complex coupling process and treat each discharge phase as independent. More accurate models to describe repetitive pulses will be extended in the future.

Acknowledgements

The authors thank the young research group in Atelier des Plasmas for fruitful discussions and the Gongfang Tech Co Ltd for technical support.

Conflicts of Interest

The authors declare no conflicts of interest.

Data Availability Statement

The data that support the findings of this study are openly available in the article.

References

1. Y. Zhu, S. Shcherbanev, B. Baron, and S. Starikovskaia, "Nanosecond Surface Dielectric Barrier Discharge in Atmospheric Pressure Air: I. Measurements and 2D Modeling of Morphology, Propagation and

Hydrodynamic Perturbations," *Plasma Sources Science and Technology* 26, no. 12 (2017): 125004.

2. S. Stepanyan, A. Y. Starikovskii, N. Popov, and S. M. Starikovskaia, "A Nanosecond Surface Dielectric Barrier Discharge in Air at High Pressures and Different Polarities of Applied Pulses: Transition to Filamentary Mode," *Plasma Sources Science and Technology* 23, no. 4 (2014): 045003.

3. S. Shcherbanev, C. Ding, S. Starikovskaia, and N. A. Popov, "Filamentary Nanosecond Surface Dielectric Barrier Discharge. Plasma Properties in the Filaments," *Plasma Sources Science and Technology* 28, no. 6 (2019): 065013.

4. A. Debien, N. Benard, and E. Moreau, "Streamer Inhibition for Improving Force and Electric Wind Produced by DBD Actuators," *Journal of Physics D: Applied Physics* 45, no. 21 (2012): 215201.

5. N. Benard and E. Moreau, "Electrical and Mechanical Characteristics of Surface AC Dielectric Barrier Discharge Plasma Actuators Applied to Airflow Control," *Experiments in Fluids* 55, no. 11 (2014): 1846.

6. D. V. Roupasov, A. A. Nikipelov, M. M. Nudnova, and A. Y. Starikovskii, "Flow Separation Control by Plasma Actuator With Nanosecond Pulsed-Periodic Discharge," *AIAA Journal* 47, no. 1 (2009): 168–185.

7. A. Y. Starikovskii, A. A. Nikipelov, M. M. Nudnova, and D. V. Roupasov, "SDBD Plasma Actuator With Nanosecond Pulse-Periodic Discharge," *Plasma Sources Science and Technology* 18, no. 3 (2009): 034015.

8. N. A. Popov, "Fast Gas Heating in a Nitrogen-Oxygen Discharge Plasma: I. Kinetic Mechanism," *Journal of Physics D: Applied Physics* 44, no. 28 (2011): 285201.

9. M. M. Nudnova, S. V. Kindysheva, N. L. Aleksandrov, and A. Y. Starikovskii, "Fast Gas Heating in N_2/O_2 Mixtures Under Nanosecond Surface Dielectric Barrier Discharge: The Effects of Gas Pressure and Composition," *Philosophical Transactions of the Royal Society A* 373, no. 2048 (2015): 20140330.

10. Y. Zhu and S. M. Starikovskaia, "Fast Gas Heating of Nanosecond Pulsed Surface Dielectric Barrier Discharge: Spatial Distribution and Fractional Contribution From Kinetics," *Plasma Sources Science and Technology* 27, no. 12 (2018): 124007.

11. L. Li and J. Wang, "Nanosecond Dielectric Barrier Discharge on a Curved Surface in Atmospheric Air: Streamer Evolution and Aerodynamic Perturbations," *Journal of Physics D: Applied Physics* 55, no. 5 (2022): 055203.

12. K. Takashima, Y. Zuzeeck, W. R. Lempert, and I. V. Adamovich, "Characterization of a Surface Dielectric Barrier Discharge Plasma Sustained by Repetitive Nanosecond Pulses," *Plasma Sources Science and Technology* 20, no. 5 (2011): 055009.

13. R. Dawson and J. Little, "Characterization of Nanosecond Pulse Driven Dielectric Barrier Discharge Plasma Actuators for Aerodynamic Flow Control," *Journal of Applied Physics* 113, no. 10 (2013): 103302.

14. K. D. Bayoda, N. Benard, and E. Moreau, "Nanosecond Pulsed Sliding Dielectric Barrier Discharge Plasma Actuator for Airflow Control: Electrical, Optical, and Mechanical Characteristics," *Journal of Applied Physics* 118, no. 6 (2015): 063301.

15. K. D. Bayoda, N. Benard, and E. Moreau, "Elongating the Area of plasma/fluid Interaction of Surface Nanosecond Pulsed Discharges," *Journal of Electrostatics* 74 (2015): 79–84.

16. F. Kong, Y. Wang, C. Zhang, X. Che, P. Yan, and T. Shao, "Electrical and Optical Characteristics of Surface Plasma Actuator Based on a Three-Electrode Geometry Excited by Nanosecond-Pulse and DC Sources," *Physics of Plasmas* 24, no. 12 (2017): 123503.

17. E. Moreau, K. Bayoda, and N. Benard, "Streamer Propagation and Pressure Waves Produced by a Nanosecond Pulsed Surface Sliding

- Discharge: Effect of the High-Voltage Electrode Shape,” *Journal of Physics D: Applied Physics* 54, no. 7 (2021): 075207.
18. K. Kourtzanidis and L. L. Raja, “Three-Electrode Sliding Nanosecond Dielectric Barrier Discharge Actuator: Modeling and Physics,” *AIAA Journal* 55, no. 4 (2017): 1393–1404.
 19. B. Peng, N. Jiang, K. Shang, N. Lu, J. Li, and Y. Wu, “Streamer Dynamics and Charge Self-Erasing of Two Counter-Propagating Plasmas in Repetitively Pulsed Surface Dielectric Barrier Discharge,” *High Voltage* 7, no. 4 (2022): 730–743.
 20. B. Peng, K. Shang, Z. Liu, et al., “Evolution of Three-Electrode Pulsed Surface Dielectric Barrier Discharge: Primary Streamer, Transitional Streamer and Secondary Reverse Streamer,” *Plasma Sources Science and Technology* 29, no. 3 (2020): 035018.
 21. B. Peng, N. Jiang, Y. Zhu, J. Li, and Y. Wu, “Three-Electrode Surface Dielectric Barrier Discharge Driven by Repetitive Pulses: Streamer Dynamic Evolution and Discharge Mode Transition,” *Plasma Sources Science and Technology* 33, no. 4 (2024): 045018.
 22. J. Hodges, J. Viallon, P. Brewer, et al., “Recommendation of a Consensus Value of the Ozone Absorption Cross-Section at 253.65 nm Based on a Literature Review,” *Metrologia* 56, no. 3 (2019): 034001.
 23. M. Nudnova and A. Starikovskiy, “Ozone Formation in Pulsed SDBD at Wide Pressure Range,” in *50th AIAA Aerospace Sciences Meeting Including the New Horizons Forum and Aerospace Exposition* (2012): 1–15.
 24. X. Qin, X. Xiao, I. K. Puri, and S. K. Aggarwal, “Effect of Varying Composition on Temperature Reconstructions Obtained From Refractive Index Measurements in Flames,” *Combustion and Flame* 128, no. 1 (2002): 121–132.
 25. M. Raffel, “Background-Oriented Schlieren (bos) Techniques,” *Experiments in Fluids* 56, no. 3 (2015): 60.
 26. Y. Zhu, Y. Wu, B. Wei, et al., “Nanosecond-Pulsed Dielectric Barrier Discharge-Based Plasma-Assisted Anti-Icing: Modeling and Mechanism Analysis,” *Journal of Physics D: Applied Physics* 53, no. 14 (2020): 145205.
 27. Y. Zhu and Y. Wu, “The Secondary Ionization Wave and Characteristic Map of Surface Discharge Plasma in a Wide Time Scale,” *New Journal of Physics* 22, no. 10 (2020): 103060.
 28. A. Kulikovskiy, “Positive Streamer in a Weak Field in Air: A Moving Avalanche-to-Streamer Transition,” *Physical Review E* 57, no. 6 (1998): 7066–7074.
 29. X. Chen, Y. Zhu, and Y. Wu, “Modeling of Streamer-to-Spark Transitions in the First Pulse and the Post Discharge Stage,” *Plasma Sources Science and Technology* 29, no. 9 (2020): 095006.
 30. B. Yin, Y. Zhu, and Y. Wu, “Modulating Sparks in a Pulse Train for Repetitive and Energy Efficient Plasma Generation,” *High Voltage* 8, no. 6 (2023): 1168–1179.
 31. Y. Zhu, X. Chen, Y. Wu, et al., “Simulation of Ionization-Wave Discharges: A Direct Comparison Between the Fluid Model and E-FISH Measurements,” *Plasma Sources Science and Technology* 30, no. 7 (2021): 075025.
 32. A. Bourdon, V. P. Pasko, N. Liu, S. Célestin, P. Ségur, and E. Marode, “Efficient Models for Photoionization Produced by Non-Thermal Gas Discharges in Air Based on Radiative Transfer and the Helmholtz Equations,” *Plasma Sources Science and Technology* 16, no. 3 (2007): 656–678.
 33. G. J. M. Hagelaar and L. C. Pitchford, “Solving the Boltzmann Equation to Obtain Electron Transport Coefficients and Rate Coefficients for Fluid Models,” *Plasma Sources Science and Technology* 14, no. 4 (2005): 722–733.
 34. L. Viehland and E. Mason, “Transport Properties of Gaseous Ions Over a Wide Energy Range,” *Atomic Data and Nuclear Data Tables* 60, no. 1 (1995): 37–95.
 35. P. Almeida, M. Benilov, and G. Benilov, “Calculation of Ion Mobilities by Means of the Two-Temperature Displaced Distribution Theory,” *Journal of Physics D: Applied Physics* 35, no. 13 (2002): 1577–1584.
 36. M. Hofmans, P. Viegas, O. V. Rooij, et al., “Characterization of a kHz Atmospheric Pressure Plasma Jet: Comparison of Discharge Propagation Parameters in Experiments and Simulations Without Target,” *Plasma Sources Science and Technology* 29, no. 3 (2020): 34003.
 37. P. Viegas, M. Hofmans, O. V. Rooij, et al., “Interaction of an Atmospheric Pressure Plasma Jet With Grounded and Floating Metallic Targets: Simulations and Experiments,” *Plasma Sources Science and Technology* 29, no. 9 (2020): 095011.
 38. S. Xiao, Y. Wang, C. Ren, et al., “Assessment on Gas-Polyethylene Terephthalate Solid Interface Partial Discharge Properties of C₄F₇N/CO₂ Gas Mixture for Eco-Friendly Gas Insulating Transformer,” *High Voltage* 9, no. 1 (2024): 35–45.
 39. C. Ding, A. Y. Khomenko, S. Shcherbanev, and S. M. Starikovskaia, “Filamentary Nanosecond Surface Dielectric Barrier Discharge. Experimental Comparison of the Streamer-to-Filament Transition for Positive and Negative Polarities,” *Plasma Sources Science and Technology* 28, no. 8 (2019): 085005.
 40. S. Shcherbanev, N. Popov, and S. M. Starikovskaia, “Ignition of High Pressure Lean H₂/air Mixtures Along the Multiple Channels of Nanosecond Surface Discharge,” *Combustion and Flame* 176 (2017): 272–284.
 41. A. Lo, A. Cessou, C. Lacour, et al., “Streamer-to-Spark Transition Initiated by a Nanosecond Overvoltage Pulsed Discharge in Air,” *Plasma Sources Science and Technology* 26, no. 4 (2017): 045012.
 42. N. Minesi, P. Mariotto, E. Pannier, G. D. Stancu, and C. O. Laux, “The Role of Excited Electronic States in Ambient Air Ionization by a Nanosecond Discharge,” *Plasma Sources Science and Technology* 30, no. 3 (2021): 035008.
 43. B. Zhang, Y. Zhu, X. Zhang, et al., “Streamer-to-Filament Transition in Pulsed Nanosecond Atmospheric Pressure Discharge: 2D Numerical Modeling,” *Plasma Sources Science and Technology* 32, no. 11 (2023): 115014.
 44. V. R. Soloviev, “Analytical Estimation of the Thrust Generated by a Surface Dielectric Barrier Discharge,” *Journal of Physics D: Applied Physics* 45, no. 2 (2012): 025205.
 45. B. Eliasson, M. Hirth, and U. Kogelschatz, “Ozone Synthesis From Oxygen in Dielectric Barrier Discharges,” *Journal of Physics D: Applied Physics* 20, no. 11 (1987): 1421–1437.
 46. M. Simeni, Y. Tang, K. Frederickson, and I. V. Adamovich, “Electric Field Distribution in a Surface Plasma Flow Actuator Powered by ns Discharge Pulse Trains,” *Plasma Sources Science and Technology* 27, no. 10 (2018): 104001.
 47. B. Peng, N. Jiang, X. Yao, et al., “Experimental and Numerical Studies of Primary and Secondary Streamers in a Pulsed Surface Dielectric Barrier Discharge,” *Journal of Physics D: Applied Physics* 52, no. 32 (2019): 325202.
 48. V. R. Soloviev and V. M. Krivtsov, “Numerical Modelling of Nanosecond Surface Dielectric Barrier Discharge Evolution in Atmospheric Air,” *Plasma Sources Science and Technology* 27, no. 11 (2018): 114001.
 49. X. Chen, Y. Zhu, Y. Wu, J. Hao, X. Ma, and P. Lu, “Numerical Investigations of Nanosecond Surface Streamers at Elevated Pressure,” *Plasma Sources Science and Technology* 30, no. 7 (2021): 075008.
 50. V. R. Soloviev, “Analytical Model of a Surface Barrier Discharge Development,” *Plasma Physics Reports* 45, no. 3 (2019): 264–276.
 51. J. Little, K. Takashima, M. Nishihara, I. Adamovich, and M. Samimy, “Separation Control With Nanosecond-Pulse-Driven Dielectric

Barrier sDischarge Plasma Actuators," *AIAA Journal* 50, no. 2 (2012): 350–365.

52. J. Zheng, Z. Zhao, J. Li, Y. D. Cui, and B. C. Khoo, "Numerical Simulation of Nanosecond Pulsed Dielectric Barrier Discharge Actuator in a Quiescent Flow," *Physics of Fluids* 26, no. 3 (2014): 036102.

53. J. Zheng, Y. Cui, Z. Zhao, J. Li, and B. C. Khoo, "Investigation of Airfoil Leading Edge Separation Control With Nanosecond Plasma Actuator," *Physical Review Fluids* 1, no. 7 (2016): 1–30.

54. J. Zheng, B. C. Khoo, Y. Cui, Z. J. Zhao, and J. Li, "Numerical Study of Control of Flow Separation Over a Ramp With Nanosecond Plasma Actuator," *International Journal of Modern Physics: Conference Series* 42 (2016): 1660151.

55. J. Zheng, J. Li, Z. Zhao, Y. D. Cui, and B. C. Khoo, "Numerical Study of Nanosecond Pulsed Plasma Actuator in Laminar Flat Plate Boundary Layer," *Communications in Computational Physics* 20, no. 5 (2016): 1424–1442.

56. S. Sato, K. Mitsuhashi, T. Enokido, A. Komuro, A. Ando, and N. Ohnishi, "Surface-Charge Control Strategy for Enhanced Electrohydrodynamic Force in Dielectric Barrier Discharge Plasma Actuators," *Journal of Physics D: Applied Physics* 54, no. 45 (2021): 455203.

57. S. B. Leonov, V. Petrishchev, and I. V. Adamovich, "Dynamics of Energy Coupling and Thermalization in Barrier Discharges Over Dielectric and Weakly Conducting Surfaces on μ s to ms Time Scales," *Journal of Physics D: Applied Physics* 47, no. 46 (2014): 465201.

58. K. Kourtzanidis, G. Dufour, and F. Rogier, "The Electrohydrodynamic Force Distribution in Surface AC Dielectric Barrier Discharge Actuators: Do Streamers Dictate the Ionic Wind Profiles?," *Journal of Physics D: Applied Physics* 54, no. 26 (2021): 26LT01.

59. C. Ren, B. Huang, B. Qi, W. Chen, and T. Shao, "Impact of Surface Charges on Energy Deposition in Surface Dielectric Barrier Discharge: A Modeling Investigation," *Plasma Sources Science and Technology* 32, no. 2 (2023): 025004.